



Rapid and large-scale synthesis of ultra-small immiscible alloy supported catalysts

Huan Zhao^a, Dan Zhang^{a,b}, Yueyue Yuan^a, Xueke Wu^a, Shaoxiang Li^b, Zhenjiang Li^c, Jianping Lai^{a,*}, Lei Wang^{a,b,**}

^a College of Chemistry and Molecular Engineering, Qingdao University of Science and Technology, Key Laboratory of Eco-chemical Engineering, Key Laboratory of Optic-electric Sensing and Analytical Chemistry of Life Science, Taishan Scholar Advantage and Characteristic Discipline Team of Eco Chemical Process and Technology, Qingdao 266042, PR China

^b College of Environment and Safety Engineering, Qingdao University of Science and Technology, Shandong Engineering Research Center for Marine Environment Corrosion and Safety Protection, Qingdao 266042, PR China

^c College of Materials Science and Engineering, Qingdao University of Science and Technology, Qingdao 266042, PR China

ARTICLE INFO

Keywords:

Incompatible alloy
Large-scale synthesis
Microwave reduction
Ultra-small sized
Electrocatalysts

ABSTRACT

It is an insurmountable challenge to synthesize carrier-supported ultra-small immiscible alloy catalyst with simple one-step method today. Here, we creatively report the first preparation of immiscible Ru-based alloys (RuRE-rGO NPs, RE=Gd, Er, Yb, La) with ~5 nm by solvent-free microwave reduction. Additionally, in alkaline electrocatalytic hydrogen evolution reaction (HER), RuGd-rGO NPs performed admirable ($\eta = 12$ mV at 10 mA cm⁻², TOF=30.6 H₂ s⁻¹ at 0.1 V), which also can be stable for 500 h even if it provides industry-related current density of 500 mA cm⁻². Density functional theory further indicates that from initial to final state of the reaction, RuGd-rGO NPs have large exothermic energy (-1.34 eV), while the dissociation energy barrier of H₂O is relatively low, causing the most likely occurrence of HER. This work provides sufficient space for the synthesis of ultra-small immiscible nano-alloy supported catalysts.

1. Introduction

Energy storage and conversion has always been an important subject of modern society's attention [1–6]. The shortage of resources and insufficient methods are serious challenges faced by scientific researchers [7–10]. Actively developing efficient and stable catalysts is the key to solving the current tense energy crisis. A satisfactory catalyst requires high intrinsic activity [11,12], a sufficient number of active sites [13–15], and strong stability [16–19], which determine the large specific surface area (such as ultra-small particles below 5 nm) [20], proper structure of the catalyst (element doping [21–23], alloy ingredients [24,25], surface modification [26–28], interfacial effects [29,30], etc.) and appropriate carrier materials (excellent conductivity, dispersion and strong interaction with active catalyst)[31] requirements. Recently, there have been numerous reports that alloying can significantly improve the activity of the catalyst, which is due to the

emergence of the second component that can effectively adjust the electronic structure [32–36]. In the development of various alloy catalysts, due to the limitations of methods to overcome the thermodynamic incompatibility between metals, researchers have to slow down the progress of immiscible alloys. For the reason that the great potential value has not been tapped yet, and the basic attributes and applications have not been widely disclosed [37–39], therefore, it is necessary to further develop general-purpose ultra-small immiscible alloys supported by carriers.

On the other hand, the synthesis of satisfactory catalysts needs to meet the following conditions: firstly, it is better to adopt a cheap and common equipment to carry out the reaction with a simple one-step method, and catalysts can be prepared on a large scale in a short time with high yield [40,41]; secondly, solvent-free could eliminate the inevitable environmental pollution problems and reduces energy consumption caused by solvents without separation process [42]. Last but

* Corresponding author.

** Corresponding author at: College of Chemistry and Molecular Engineering, Qingdao University of Science and Technology, Key Laboratory of Eco-chemical Engineering, Key Laboratory of Optic-electric Sensing and Analytical Chemistry of Life Science, Taishan Scholar Advantage and Characteristic Discipline Team of Eco Chemical Process and Technology, Qingdao 266042, PR China

E-mail addresses: jp lai@qust.edu.cn (J. Lai), inorchemwl@126.com (L. Wang).

<https://doi.org/10.1016/j.apcatb.2021.120916>

Received 19 August 2021; Received in revised form 21 October 2021; Accepted 7 November 2021

Available online 20 November 2021

0926-3373/© 2021 Elsevier B.V. All rights reserved.

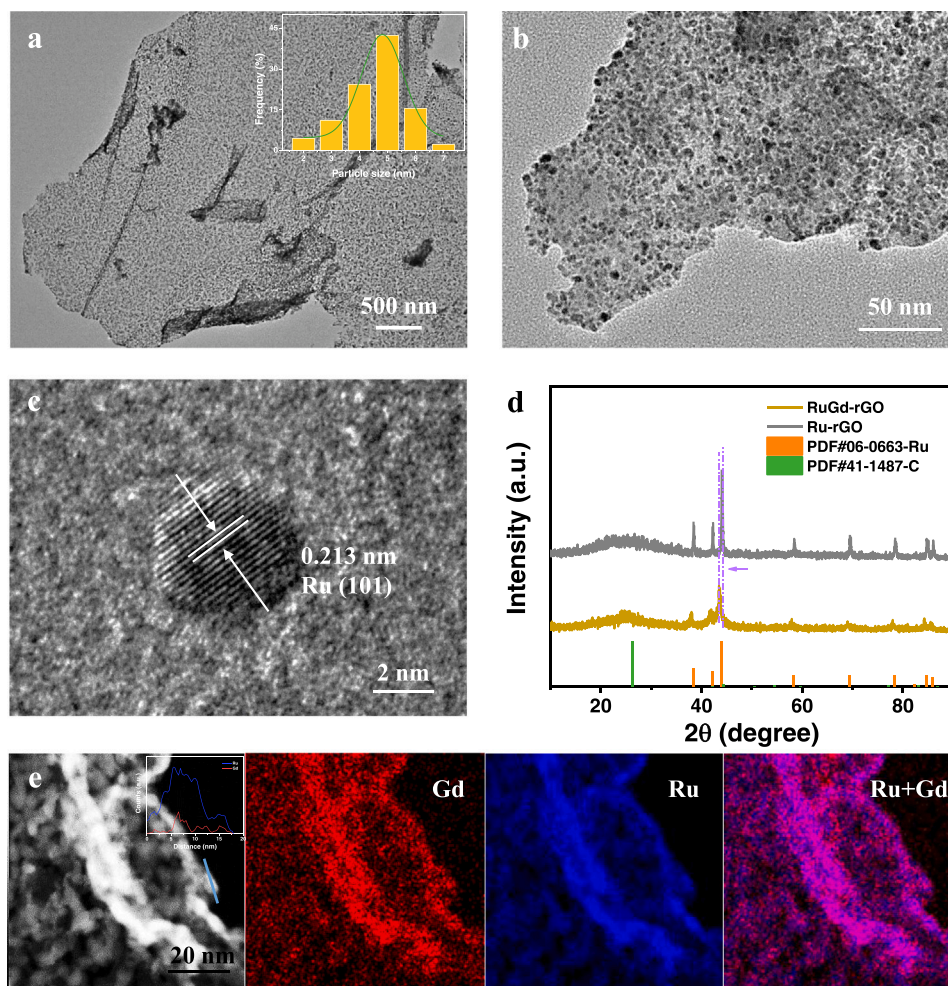


Fig. 1. Morphological and structural characterizations of RuGd-rGO NPs. (a, b) TEM images (insert: size distribution). (c) HRTEM image. (d) XRD patterns of RuGd-rGO NPs and Ru-rGO NPs. (e) HAADF-STEM image and corresponding EDX elemental mapping (insert: line scan showing Ru and Gd distributions along the line marked).

not least, it is pleasant if the self-reduction of the medicine can be achieved without introducing a strong reducing agent, which is economic and effective. However, in fact, it is still an arduous task to explore a universal method that takes into account the above items.

Finally, considering that ruthenium (Ru) is a promising electrocatalyst that has aroused great interest, we chose Ru as the observation site [43]. On the one hand, the price of Ru is only 1/3 of platinum (Pt), and it is an economical replacement HER electrocatalyst of Pt. On the other hand, the Gibbs free energy of the Ru-H bond is very close to the Pt-H bond (optimum) in the center of the volcano map, and they also have similar bond strength (about 65 kcal mol⁻¹), so that it has potential HER activity comparable to Pt [44,45]. Therefore, we integrated the above viewpoints and chosen to design and synthesize a brand new ultra-small alloy materials (RuRE-rGO NPs, RE=Gd, Er, Yb, La) in a household microwave oven, which is the first preparation of Ru-RE materials, overcoming the huge gap between the standard reduction potentials of metals and the high affinity for oxygen. In this contribution, we synthesized the alloy of Ru and rare earth metals by solvent-free microwave thermal method, which is difficult to form conventionally, and dispersed on the rGO substrate to obtain a catalyst with large specific surface area and ultra-small particles. Moreover, it can be prepared on a gram scale in a short time with high yield rate, reflecting the feasibility of large-scale production. According to experimental verification, RuGd-rGO NPs have superior performance in alkaline electrocatalytic HER, with low overpotential and high turnover frequency

(TOF), much superior to commercial Pt/C, becoming one of the most advanced HER electrocatalysts (Tables S1-S3). Even in the high current test, it could rely on amazing 56 and 108 mV to reach the current density of 500 and 1000 mA cm⁻², fully qualified for industrial-grade applications (Table S4). Due to the introduction of RE atoms with unique electronic structure, the catalyst is extremely stable and robust even working for 500-hour chronoamperometry test. The synthesis and application of ultra-small immiscible alloy catalysts supported by carrier with microwave self-reduction described in this work provides major guiding significance for the future development of such catalysts.

2. Experimental section

2.1. Materials synthesis

2.1.1. Pre-processing of rGO

40 mg GO powder was dissolved in 80 mL N,N-dimethylformamide (DMF) containing 2 mL ammonia solution, sealed and ultrasonicated for one hour to form a homogeneous solution. Finally, condensate and reflux in an oil bath at 150 °C for 3 h to obtain reduced graphene oxide.

2.1.2. Synthesis of RuGd-rGO NPs

First, 18.5 mg treated rGO, 2.5 mg Gd(NO₃)₃·6H₂O, and 16 mg Ru₃(CO)₁₂ were mixed, and ground in a mortar for more than 30 min for uniform mixing. Then, the mixture was put into a 10 mL quartz glass vial

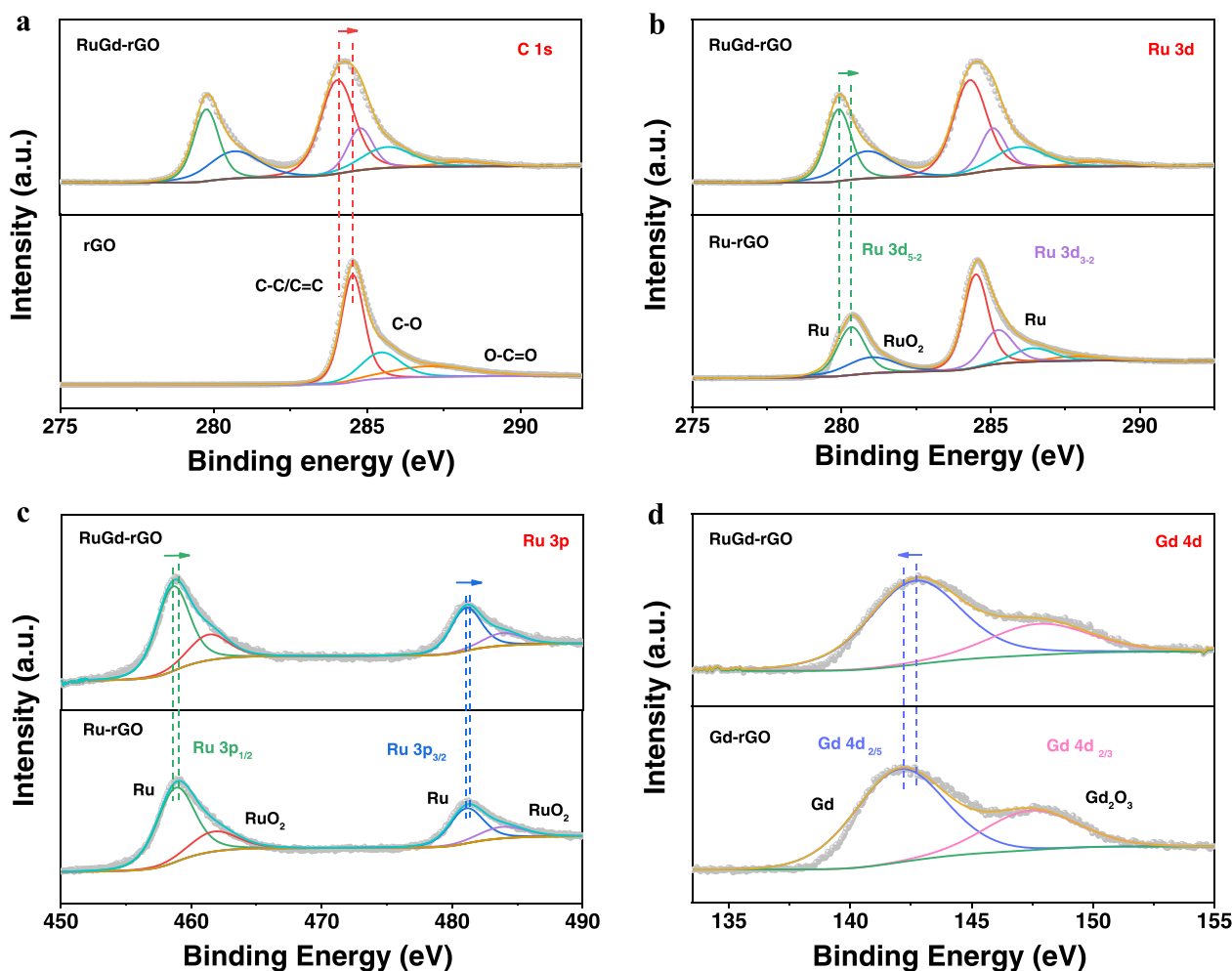


Fig. 2. XPS spectra of RuGd-rGO NPs. (a) C 1 s of RuGd-rGO NPs and rGO. (b) Ru 3d of RuGd-rGO NPs and Ru-rGO NPs. (c) Ru 3p of RuGd-rGO NPs and Ru-rGO NPs. (d) Gd 4d of RuGd-rGO NPs and Gd-rGO.

and irradiated in a household microwave oven for 60 s

The synthesis methods of RuGd-rGO NPs with different rGO ratios are as follows. The operation steps are the same as the previous description, except that the amounts of rGO added are 9.3 mg and 37 mg, respectively.

As for the synthesis of RuGd-rGO NPs with different metal proportions, the operation steps are the same as the previous description, except that the amounts of rGO added are 1.1 mg and 4.5 mg, respectively.

2.1.3. Synthesis of Ru-rGO NPs

The operation steps are consistent with RuGd-rGO NPs, except for the loss of Gd(NO₃)₅·6 H₂O participation.

2.1.4. Synthesis of RuRE-rGO NPs

2.5 mg Gd(NO₃)₅·6H₂O was replaced as 2.3 mg Er(NO₃)₅·6H₂O, 2.3 mg Yb(NO₃)₅·5 H₂O, and 2.2 mg La(NO₃)₅·6 H₂O, respectively. Other operation steps are consistent with the above.

2.2. Materials characterizations

Transmission electron microscopy (TEM) and energy-dispersive X-ray spectroscopy (EDX) elemental mapping were used to characterize the morphologies of the catalysts and spatial distribution of elements on a JEM-F200 with the accelerating voltage of 200 kV. Furthermore, scanning electron microscopy (SEM) was utilized to show structure of the

catalysts on the Regulus8100 and its accelerating voltage was set as 10 kV. X-ray diffraction (XRD) analysis was recorded on X'Pert PRO MPD at a scanning rate of 1° min⁻¹ in the 2θ ranges from 5° to 90°. X-ray photoelectron spectroscopy (XPS) measurements were operated to insure the superficial chemical states by the AXIS SUPRA with a monochromatic Al Kα source at 15 mA and 14 kV. Scan analysis with an analysis area of 300 × 700 μm and a pass energy of 100 eV. The spectrum was calibrated by carbon 1 s spectrum, and its main line was set to 284.6 eV. The compositions of catalysts were determined by the inductively coupled plasma atomic emission spectrometer (ICP-AES) that is Varian 710-ES for better accuracy. The catalyst after stability test was scraped from the working electrode by ultrasonic treatment and collected for the next TEM and XRD characterization.

2.3. Electrochemical measurements

Electrochemical measurements were conducted on a CHI760 Electrochemical Workstation (Shanghai Chenhua Instrument Corporation, China) in a conventional three-electrode cell by using a carbon rod as the counter electrode and a saturated calomel electrode as the reference electrode. The working electrode was a glassy carbon electrode (GCE, diameter: 3 mm, area: 0.07065 cm²). The synthesized catalysts were dispersed in ethanol + 5% Nafion (v:v=1:0.02) to reach a homogeneous catalyst ink with a concentration of 1 mg mL⁻¹ by sonicating for 1 h. Then, 10 μL ink was dropped onto the surface of the GCE for further electrochemical tests (the load of NF: 0.5 mg cm⁻²). In the overall RuGd-

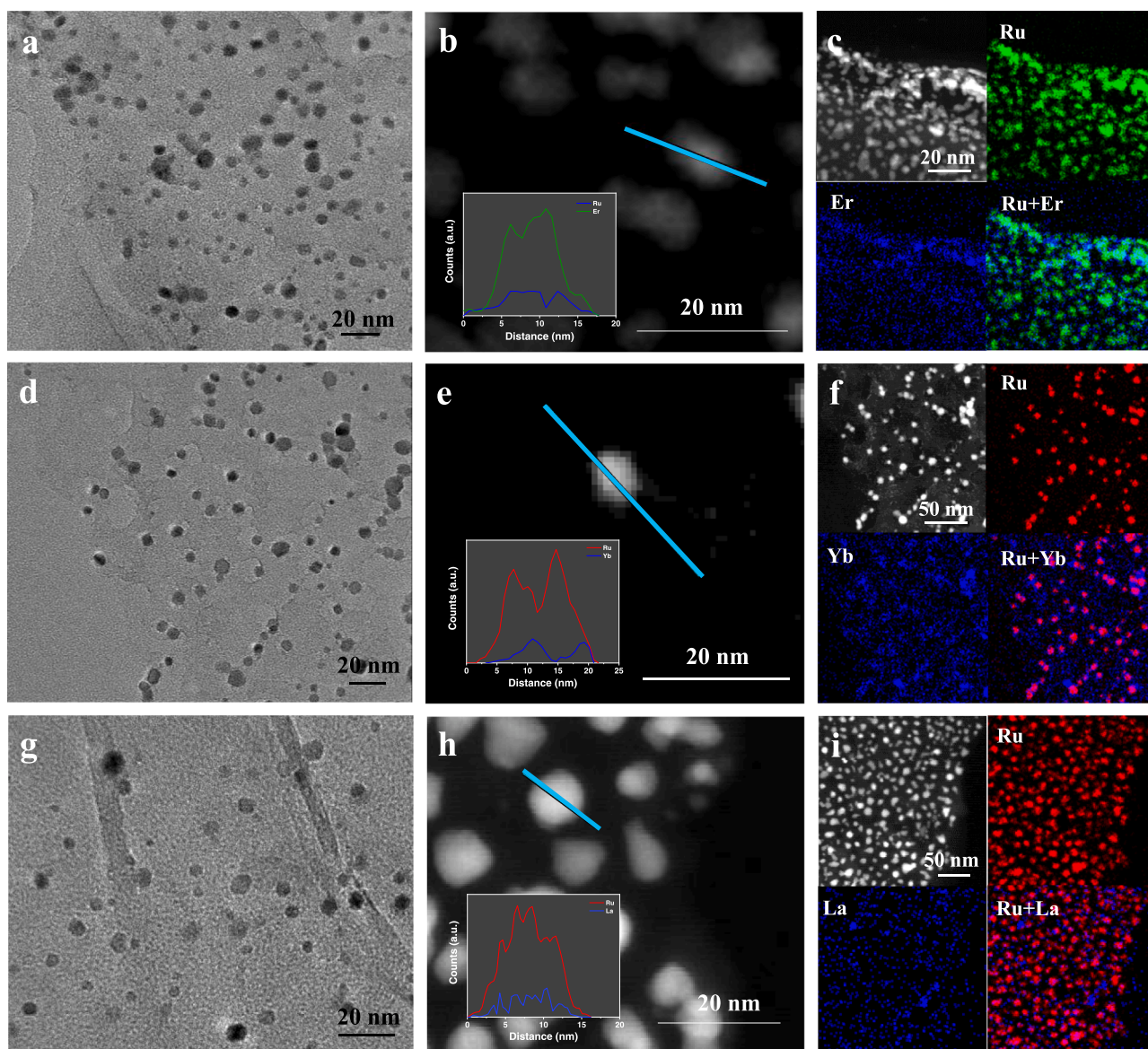


Fig. 3. Characterizations of other RuRE-rGO NPs. (a, d, j) TEM images, (b, e, h) HAADF-STEM images and the corresponding EDX line scan, (c, f, i) HAADF-STEM images and the corresponding EDX elemental mapping of RuEr-rGO, RuYb-rGO and RuLa-rGO NPs.

rGO catalyst, the mass contents are as follows: Ru: 5.45 wt%; Gd: 1.13 wt%. The HER measurements were performed in 1.0 M KOH saturated with N_2 solution using GCE. The polarization curves were obtained at a scan rate of 5 mV s^{-1} and corrected for 95% iR. All potentials reported in this work are corrected using reversible hydrogen electrodes. The active sites were measured by Cu-UPD method. A new CV at a sweep rate of 10 mV s^{-1} over a range of 0–0.8 V is scanned to obtain a background curve for correcting the charge associated with any background processes. Then, a rated voltage is applied to the working electrode for 100 s to form the Cu-UPD monolayer in 0.5 M H_2SO_4 contained 5.0 mM $CuSO_4$. The Cu-UPD stripping voltammograms are obtained by sweeping the working-electrode voltage from 0.23 to 0.26 V at a sweep rate of 10 mV s^{-1} . Chronoamperometry test and 1 0,000 cycles of CV was used to evaluate the stability of the catalyst in 1.0 M KOH solution. Electrochemical impedance spectroscopy (EIS) measurement was performed at a frequency of 0.1 Hz to 100 kHz under -0.022 V vs. RHE in a 1.0 M KOH.

3. Results and discussion

3.1. Fabrication and physical characterization

As for the fabrication of RuRE-rGO NPs, at first, the Ru salt and RE metal hydrate are mixed, milled together with rGO. Soon afterwards, RuRE alloy NPs loaded with rGO were reduced by microwave reaction for only one minute in the special vial made of quartz glass (Fig. S1), and the rapid completion of the reaction is because the materials can absorb microwaves and heat at the same time both inside and outside. Under the multiple interaction of the external microwave field and the carbon material, the carbonyl salt rapidly undergoes thermal conversion and decomposition into CO gas, so that the metal ions are rapidly reduced to nanoparticles in a limited space and attached to the rGO. At this time, rGO interacts with metal under strong microwave radiation, resulting in strong metal-support interaction (SMSI). SMSI can not only prevent the agglomeration of loaded nanoparticles and promote the electron transfer process between the carrier and the load, but also make the load firmly anchored on the carrier, improving the stability of the material

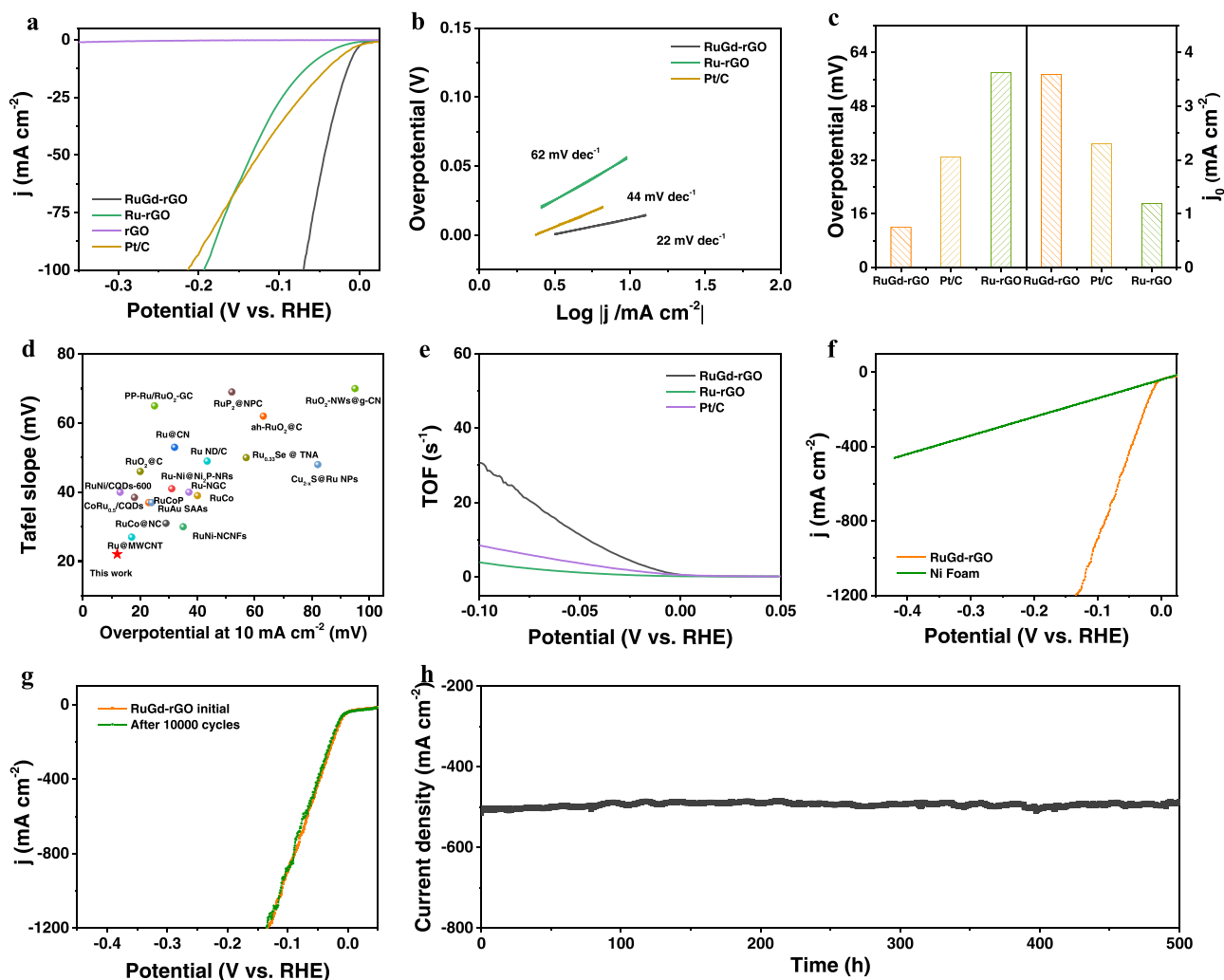


Fig. 4. HER catalytic performance in 1.0 M KOH. (a) HER polarization curves. (b) Tafel slopes of RuGd-rGO, Ru-rGO NPs, rGO and Pt/C. (c) Overpotentials ($j = 10 \text{ mA cm}^{-2}$) and exchange current density (j_0) of RuGd-rGO, Ru-rGO NPs and Pt/C. (d) Comparison with different representative electrocatalysts under alkaline media. (e) TOF values of RuGd-rGO, Ru-rGO NPs and Pt/C. (f) Polarization curves of RuGd-rGO/NF and pure NF under large current. (g) Polarization curves of RuGd-rGO/NF after the 1st and 10,000th cycles. (h) The current-time curve of RuGd-rGO/NF at the potential required to maintain 500 mA cm^{-2} for 500 h.

[33,46]. RGO is the carrier, which enhances the overall conductivity and dispersion of the material. The reaction products can be obtained quickly by a simple one-step method, greatly simplifies the procedure and saves time. The high-temperature microwave reduction simultaneously acts internally and externally to quickly sinter the reaction into the desired fusion phase; at the same time, the shorter sintering time limits the size of the particles ($\sim 5 \text{ nm}$). It can be seen from Fig. S2, scanning electron microscope (SEM) and transmission electron microscopy (TEM) show that the treated rGO is an ultra-thin layered structure with wrinkles on the surface, which determines the large surface area of the materials. The X-ray diffraction (XRD) pattern was provided in Fig. S3. As we can see from Fig. 1a and b, the RuGd-rGO NPs synthesized by this microwave method have ultra-small size about 4.6 nm shown in the size distribution diagram in Fig. 1a, and the unanimous conclusion can also be drawn in the high resolution transmission electron microscope (HRTEM). The lattice spacing is 0.213 nm , which corresponds to the Ru (101) plane (Fig. 1c). Although the corresponding lattice of Gd is not found in the HRTEM image, we guess that Gd is doped into the Ru lattice fringes to cause the subsequent lattice expansion. The intensive diffraction peaks of pure Ru-rGO are located at 38.4° , 42.2° and 44.0° , matching the (100), (002) and (101) planes of hexagonal Ru, respectively (Fig. 1d). For RuGd-rGO, the presence of Gd is not nearly observed, but the Ru peaks are broadened and the intensity is reduced

due to the incorporation of Gd atoms. Simultaneously, the diffraction peaks of RuGd-rGO shifted to a certain extent, again verifying the formation of RuGd alloy. In addition, energy-dispersive X-ray spectroscopy (EDX) element mappings and line scan further confirmed the uniformly distributed in space of Ru and Gd elements in the catalyst, constituting the alloy structure (Fig. 1e and Fig. S4).

To further clarify the element valence states and the bonding states of RuRE-rGO, X-ray photoelectron spectroscopy (XPS) was used for characterization and analysis. We took RuGd-rGO as an example, and selected Ru-rGO and rGO as references to explore. The survey spectra were listed in Fig. S5, we can see the presence of elements in RuGd-rGO, and the successful synthesis of the certified material is also verified from another aspect. The high-resolution XPS spectrum of C 1s can be divided into three peaks (Fig. 2a). The peaks at 284.6 eV , 285.5 eV , and 287.0 eV are attributed to $\text{C}=\text{C}/\text{C}-\text{C}$, $\text{C}-\text{O}$ and $\text{O}=\text{C}-\text{O}$, respectively [47]. Compared with pure rGO, the binding energy of RuGd-rGO has shifted to high binding energy by 0.2 eV , which means that there has been charge transfer between the active material RuGd and the base material rGO. SMSI phenomenon can be further verified by XPS analysis. As shown in Fig. 2b, the characteristic peaks of Ru 3d and C 1s slightly overlap, and Ru $3d_{5/2}$ and Ru $3d_{3/2}$ are located at binding energies of 280.3 eV and 285.2 eV , respectively [48,49]. In addition, a characteristic peak of RuO_2 was found at 281.0 eV . Ru 3p can be resolved into

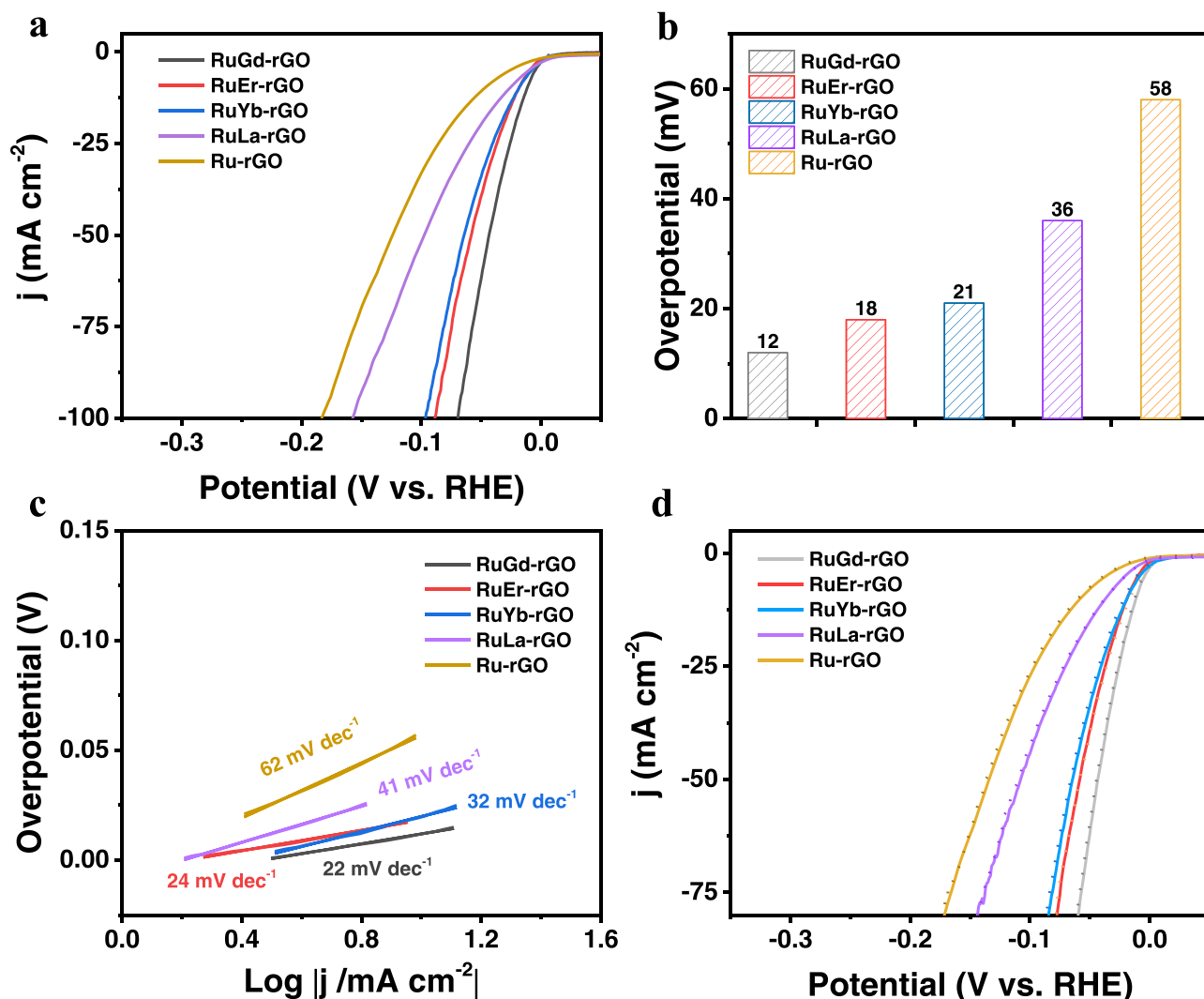


Fig. 5. HER catalytic performance of RuRE-rGO NPs. (a) Polarization curves. (b) Overpotentials at $j = 10 \text{ mA cm}^{-2}$. (c) Tafel slopes. (d) Polarization curves of RuRE-rGO NPs before and after 10,000th cycles (solid line: before 10,000th cycles; dotted line: after 10,000th cycles).

four peaks in Fig. 2c, including most of the metal states (461.7 eV and 484.1 eV) and a little amount of oxidation states (464.5 eV and 486.7 eV) caused by long-term exposure to the air [47,50,51]. Through the analysis of the peak positions about Ru element in Ru-rGO and RuGd-rGO, it is found that Ru in RuGd-rGO shifts to a higher binding energy direction, indicating that the introduction of Gd element causes the charge transfer between the two metal components. Correspondingly, Gd 4d of RuGd-rGO and Gd-rGO were analysed in Fig. 2d. Notably, there are localized electrons in the 4f shell of lanthanide metals, so that a typical characteristic Gd XPS is generally quite complex, resulting in a broad and multi-state structure [52]. The broad peak at 142.2 eV is attributed to the metallic state of Gd-rGO, and the adjacent short peak is attributed to the oxidation state [53]. Generally, the presence of small amounts of oxides is common, which can be explained by the ultra-low reduction potential of rare earth elements and long-term contact with oxygen in the air. Simultaneously, compared with single metal Gd, the binding energy of RuGd-rGO is significantly negatively shifted. The above data reveals that charge transfer between the carrier rGO and the alloy composition Ru-Gd, further realizing a strong bond between the substrate and the alloy; in addition, the shift of the metal peaks analyzed by XPS also proves that there is also a flow of electrons between Ru and Gd, and finally formed uniform alloy material. The ubiquitous electron transfer phenomenon in the catalyst contributes

to the occurrence of favorable electrocatalytic activity. In addition, XPS can be applied to roughly evaluate the content of each element, which is consistent with the results measured by inductively coupled plasma atomic emission spectrometer (Ru: 82.8%, Gd: 17.2%).

In addition to RuGd-rGO NPs, we extend the synthetic method to RuEr-rGO, RuYb-rGO, and RuLa-rGO NPs with ultra-small size ($\sim 5 \text{ nm}$). Then a series of physical characterizations such as TEM, EDX line scan and elemental mapping described the existence state and element distribution of RuRE-rGO NPs (Fig. 3). In addition, the cooperative analysis of XRD and XPS further confirmed the synthesis of alloy nanoparticles, and Figs. S6–13 reveal the general applicability of microwave reduction to immiscible alloys.

3.2. Electrocatalytic application

The electrocatalytic hydrogen evolution of RuRE-rGO NPs was first evaluated in a three-electrode system. The polarization curve was measured in 1.0 M KOH saturated with N_2 , and Ru-rGO NPs and rGO were detected as a reference. According to Fig. 4a, it is clear that RuGd-rGO NPs has a larger current density and a smaller onset potential (near zero), which is significantly better than commercial Pt/C. In particular, the current density of RuGd-rGO NPs increased rapidly with the increasing voltage, which left a deep impression. The overpotential is

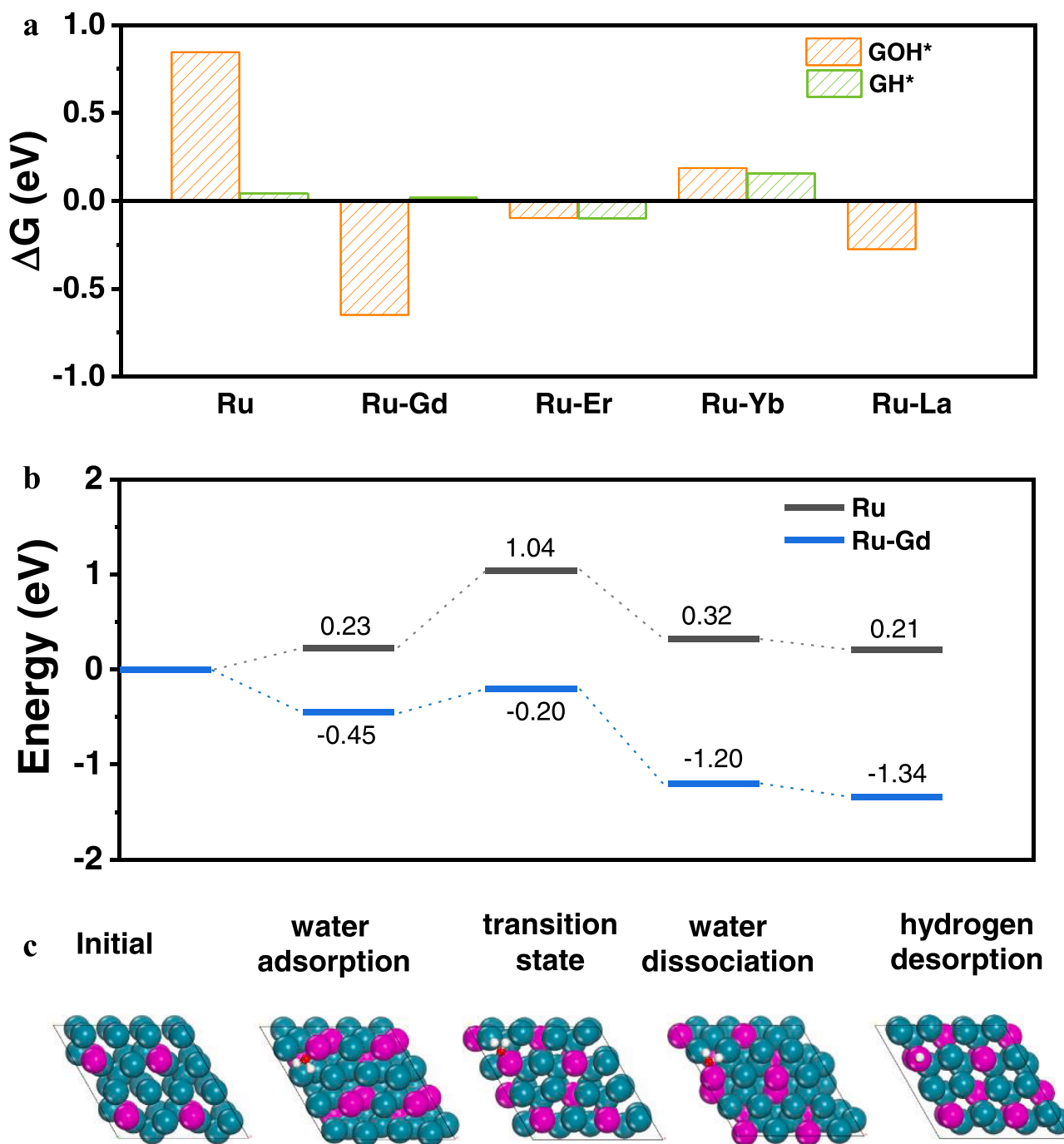


Fig. 6. Density functional theory calculations for Ru and Ru-RE. (a) Calculated H-binding energies (ΔG_{H^*}) and OH-binding energies (ΔG_{OH^*}) for Ru and Ru-RE surfaces. (b) Gibbs free energy profiles for alkaline HER on Ru and Ru-Gd surfaces. (c) At each stage of the reaction path, the bonding model of Ru-Gd surface.

only 12 mV at the current density of 10 mA cm^{-2} , while Pt/C and Ru-rGO are 33 mV and 58 mV, respectively (Fig. 4c), which is almost the lowest than ever reported (Table S3). We also made a statistical comparison of the overpotentials of the three materials at 20, 50, and 100 mA cm^{-2} in Fig. S14. The results show that as the current density increases, the overpotentials of the three materials all show an upward trend, but in terms of the increase rate, RuGd-rGO NPs is the slowest, which once again proves the desirable activity. Especially under high current, RuGd-rGO NPs provide a prerequisite for subsequent practical applications. Meanwhile, rGO has no additional performance, indicating that its active components are indeed derived from the nanoparticles it supports. Compared with Ru-rGO NPs, the superior performance of RuRE-rGO NPs is attributed to the alloy structure, which proves that the

introduction of RE elements can promote HER effectively. The corresponding Tafel slope is shown in Fig. 4b. The Tafel slope of RuGd-rGO NPs is only 22 mV dec^{-1} , which is lower than Ru-rGO NPs (62 mV dec^{-1}), conforming to the Volmer-Tafel mechanism. The exchange current density (j_0) can be obtained by extrapolating the Tafel diagram (Fig. 4c). The j_0 of Ru-rGO NPs is 3.6 mA cm^{-2} , which is much higher than that of Pt/C (2.3 mA cm^{-2}) and Ru-rGO NPs (1.2 mA cm^{-2}). Fig. 4d tells us RuGd-rGO NPs have an absolute advantage over most noble metal HER catalysts (including Pt-based and Ru-based) and non-noble metal catalysts in terms of HER activity. Next, electrochemical impedance spectroscopy (EIS) measurement was carried out, and the semicircle in the middle frequency range reflected the charge transfer resistance (R_{ct}). Compared with Ru-rGO, the introduction of RE atoms

into the Ru matrix brings about a smaller R_{ct} (Fig. S15). This drives the charge transfer process of RuRE-rGO NPs, which is conducive to improving HER kinetics. Furthermore, electrochemical double-layer capacitance (C_{dl}) is used to evaluate the active area of the catalyst. As we can see in Fig. S16, RuGd-rGO NPs (9.94 mF cm^{-2}) are twice than Ru-rGO NPs (5.81 mF cm^{-2}), and the electrochemically active surface area (ECSA) is derived from this (Fig. S17), in which RuGd-rGO NPs reached $176 \text{ m}^2 \text{ g}^{-1}$. Subsequently, the current density was renormalized by ECSA. From Fig. S18, it can be clearly observed that the HER activity of Ru-rGO NPs is much lower than RuGd-rGO NPs although the ECSA of RuGd-rGO NPs is larger than Ru-rGO NPs, which fully reflects the inherent high activity of RuGd-rGO NPs derived from itself. Actually, Cu-underpotential deposition (Cu-UPD) is also suitable for the evaluation of catalyst surface area (Fig. S19), which is also consistent with the above-mentioned ECSA. Turnover frequency (TOF), one of the important indicators for evaluating the potential activity of catalyst, is further calculated by the obtained number of active sites from Cu-UPD (Fig. S20). It can be seen from Fig. 4e that the TOF of RuGd-rGO NPs exhibits ultra-high hydrogen evolution intensity overall. The TOF value of RuGd-rGO NPs reached $30.6 \text{ H}_2 \text{ s}^{-1}$ at 0.1 V, which is in the leading position among the currently reported catalysts (Table S4), far superior to Pt/C ($8.5 \text{ H}_2 \text{ s}^{-1}$) and Ru-rGO NPs ($3.9 \text{ H}_2 \text{ s}^{-1}$).

It has been verified that the immiscible alloy nanoparticles supported by rGO can be reduced by microwave, which could be easily and quickly prepared on a large scale and high yield of 82.1% without affecting the morphology and size, indicating that the materials prepared by this method have potential practical industrial value (Fig. S21). Considering that industrial hydrogen evolution generally requires a large current density, the RuGd-rGO NPs were fixed on foamed nickel (NF) in 1.0 M KOH solution for testing. It turns out that the overpotentials of RuGd-rGO/NF can reach astonishing 56 mV and 108 mV at the current density of 500 and 1000 mA cm^{-2} (Fig. 4f), respectively, which is far lower than the blank NF and superior to all previously reported materials (Table S5), showing unprecedented high current activity and application potential. The stability of the material is the key to measuring whether it has the potential for long-term use. After 10,000 cycles of CV test, the polarization curve did not attenuate (Fig. 4g). In addition, the chronoamperometric measurement showed that even after working 500 h, the current density of catalyst remained stable at a potential of 56 mV (Fig. 4h). After the long-term stability reaction, the morphology and structure of the catalyst were characterized here. Fig. S22a shows a TEM image, of which small-sized nanoparticles are enriched on rGO, and the morphology has not changed significantly. Moreover, the XRD pattern is consistent with the characteristic peak before the reaction in Fig. S22b. As shown in Fig. S23, XPS analysis also shows that the state of each element is consistent with the previous one. In addition, Fig. S24 shows the chronopotentiometric curve of the RuGd-rGO/NF at a constant current density of 500 mA cm^{-2} for 500 h, and the result further prove the high stability of RuGd-rGO/NF. The above signs point to the highly stable existence of the catalyst. The long-lasting durability of the catalyst is mainly due to the reconciliation effect of RE elements, that is, the negative formation energy of Ru-RE contributes to the stability of the material. Therefore, they are more stable naturally in terms of electronic and structural effects than other materials.

3.3. Material optimization and expansion

In order to stimulate the best state of the catalyst, the composition and ratio have been regulated regularly. Firstly, the amount of carrier (rGO) added is considered as the research object. Based on the 1:1 mass ratio of RuGd and rGO, the HER activity changes of RuGd-rGO NPs were studied after adding a small amount (2:1) and an excessive amount (1:2) of rGO, respectively. In Fig. S25, the electrocatalytic parameters were characterized. When the polarization curve shows a ratio of 1:1, the current density of RuGd-rGO NPs is the largest. The overpotential is the lowest, and the Tafel slope is also the smallest. After determining the

appropriate addition amount of the active component and the carrier, the ratio of Ru salt and RE salt is adjusted in the next step. We tried the following materials $\text{Ru}_{83}\text{Gd}_{17}$ -rGO, $\text{Ru}_{72}\text{Gd}_{28}$ -rGO and $\text{Ru}_{91}\text{Gd}_9$ -rGO, and the content of elements was preliminary quantified by XPS (Fig. S26). It has been verified that all the three performed well, with similar Tafel slopes and overpotentials. Among them, $\text{Ru}_{83}\text{Gd}_{17}$ -rGO was found to have the best properties (Fig. S27). In addition, we quantified the actual H_2 production of $\text{Ru}_{83}\text{Gd}_{17}$ -rGO NPs by gas chromatography (GC), which has hardly any difference from the theoretical hydrogen production (Fig. S28). The Faradaic efficiency is close to 100%, reflecting the high selectivity to H_2 . By optimizing the various components of the material, the ability of RuRE-rGO NPs to promote hydrogen evolution has been further improved.

A series of electrochemical performances of RuRE-rGO NPs are provided, as shown in Fig. 5. From Fig. 5a, the polarization curves of RuRE-rGO NPs show the wonderful HER activity, and the overpotentials at 10 mA cm^{-2} are listed in Fig. 5b, which indicates low starting potentials compared with Ru-rGO NPs. Moreover, the corresponding Tafel slopes and EIS reveal the favorable electron transfer and hydrogen evolution kinetics (Fig. 5c and Fig. S29a). Then, the specific surface area of the catalyst is roughly estimated by C_{dl} (Fig. S29b), which is known to be proportional to ECSA, corresponding to Fig. S29c. And we can see, RuRE-rGO NPs are ahead of Ru-rGO NPs in surface area due to the participation of RE elements, providing a basis for subsequent electrocatalysis. Finally, it is noteworthy that the polarization curves of RuGd-rGO NPs after 10,000 cycles of cyclic voltammetry test still basically overlap with almost no loss of activity in Fig. 5d. The same situation is also appeared in other RuRE-rGO NPs, thus proving the extraordinary stability of RuRE-rGO NPs. The above results all show that RuRE-rGO NPs is one of the most advanced HER catalysts due to the introduction of RE elements to form a unique alloy structure, which puts forward a new idea for further realization of future industrial applications.

3.4. Theoretical calculation

For exploring the mechanism of RuRE-rGO on alkaline HER in depth, density functional theory (DFT) is based on the Gibbs free binding energy of hydrogen (ΔG_{H^*}) and hydroxide ion (ΔG_{OH^*}), the surface free energy of the catalyst in the reaction process to explain. Fig. 6a exhibits the ΔG_{H^*} and ΔG_{OH^*} of Ru and Ru-RE, and the definite values are given in Table S6. As shown in the picture, the participation of RE atoms significantly reduces the binding energy of OH^* , making the dissociation state of water more stable. In addition, from the experimental measurement of overpotential and Tafel slope as a function of ΔG_{H^*} , the volcano relationship is obtained. As shown in Fig. S30, it is revealed that RuGd-rGO has an optimal ΔG_{H^*} value in the volcano graph, reflecting the moderate energy of the active catalyst for the adsorption of the intermediate. Furthermore, the binding energy of H^* on Ru-Gd is infinitely close to 0, at a near perfect ΔG_{H^*} , thereby improving the H^* -binding ability. Appropriate H^* and OH^* combination willingness fundamentally promotes alkaline HER.

Then, in order to further explore the reasons for the excellent activity of Ru-Gd in alkaline environment, the reaction path in the whole HER process was split: water adsorption, dissociation and hydrogen desorption. As shown in Fig. 6b and c, the Gibbs free energy on each intermediate is listed separately. In the process of water dissociation, exothermic energy of 1.1 eV on Ru-Gd verifies the process is the rate-determining step of the reaction process, again indicating that the entire HER kinetics is controlled by Volmer step. The total exothermic energy of Ru-Gd reached 1.34 eV, which is 0.51 eV higher than pure Ru. Coupled with the low dissociation energy barrier of H_2O , HER is relatively more likely to occur for Ru-Gd. In addition, the Gibbs free energy profiles on each intermediate of the other Ru-RE are listed in Fig. S31, and the definite values of basic HER for each transition state on the surface of Ru and Ru-RE are included in Table S7. Although the ΔG_{H^*} and ΔG_{OH^*} of Ru-La are in a decent state, the excessively high H_2O

dissociation energy barrier causes it to be slightly inferior to the other three in terms of alkaline HER performance. Nevertheless, it is still superior to the performance of pure Ru. Figs. S32–35 exhibit the modes of Ru and Ru-RE at each stage of the reaction path. Therefore, the appearance of RE atom gives Ru the most suitable Gibbs free binding energy, which is conducive to the dissociation and adsorption of water molecules, thus accelerating the entire HER dynamic process.

4. Conclusions

In summary, we prepared carrier-supported ultra-small immiscible alloy RuRE-rGO NPs (RE=Gd, Er, Yb, La) with a simple one-step method, and the reaction was controlled to complete within 60 s. What is impressive is RuGd-rGO NPs has an ultra-small particle size (4.6 nm) and a large electrochemically active surface area ($176 \text{ m}^2 \text{ g}^{-1}$), thereby exhibiting extremely outstanding performance in the alkaline electrocatalytic hydrogen evolution reaction. It only needs an ultra-low overpotential of 12 mV to achieve the current density of 10 mA cm^{-2} and the TOF value representing intrinsic activity is as high as $30.6 \text{ H}_2 \text{ s}^{-1}$ at 0.1 V, which has become one of the most advanced HER electrocatalysts. In addition, the catalyst can be synthesized in a large area on the scale of grams with almost no loss, and it was found to provide industry-relevant high current densities of 500 and 1000 mA cm^{-2} at the unprecedented low overpotentials of 56 mV and 108 mV, respectively. It is worth mentioning that the material is extremely stable and robust regardless of the stability test of the 10000-cycle cyclic voltammetry (CV) test or the 500-hour chronoamperometry test. Density functional theory (DFT) further indicates that from the initial state to the final state of the reaction, RuGd-rGO NPs have a large exothermic energy (-1.34 eV), and the dissociation energy barrier of H_2O is relatively low, which leads to the most likely occurrence of HER. This work provides a new and reliable idea for the effective synthesis and large-scale preparation of ultra-small immiscible alloy catalysts supported by carrier, and also introduces an efficient and stable catalyst for the electrocatalysis field.

CRediT authorship contribution statement

Huan Zhao: Investigation, Data curation, Conceptualization, Formal analysis, Validation, Writing – original draft. **Dan Zhang:** Formal analysis, Data curation, Validation, Writing – original draft. **Yueyue Yuan:** Data curation, Conceptualization, Validation. **Xueke Wu:** Formal analysis. **Shaoxiang Li:** Validation. **Zhenjiang Li:** Validation. **Jianping Lai:** Conceptualization, Writing – review & editing, Supervision, Funding acquisition. **Lei Wang:** Writing – review & editing, Funding acquisition, Supervision.

Declaration of Competing Interest

The authors declare that they have no known competing financial interests or personal relationships that could have appeared to influence the work reported in this paper.

Acknowledgement

This work was supported by the National Natural Science Foundation of China (51772162, 22001143 and 52072197), Youth Innovation and Technology Foundation of Shandong Higher Education Institutions, China (2019KJC004), Outstanding Youth Foundation of Shandong Province, China (ZR2019JQ14), Taishan Scholar Young Talent Program (qtsn201909114, tsqn201909123), Natural Science Foundation of Shandong Province (ZR2020YQ34), Major Scientific and Technological Innovation Project (2019JZZY020405), and Major Basic Research Program of Natural Science Foundation of Shandong Province under Grant (ZR2020ZD09).

Appendix A. Supporting information

Supplementary data associated with this article can be found in the online version at doi:10.1016/j.apcatb.2021.120916.

References

- [1] S. Chu, A. Majumdar, Opportunities and challenges for a sustainable energy future, *Nature* 488 (2012) 294–303, <https://doi.org/10.1038/nature11475>.
- [2] H.A. Gasteiger, N.M. Marković, Just a dream—or future reality? *Science* 324 (2009) 48–49, <https://doi.org/10.1126/science.1172083>.
- [3] Y. Zhao, L. Zhang, J. Liu, K. Adair, F. Zhao, Y. Sun, T. Wu, X. Bi, K. Amine, J. Lu, X. Sun, Atomic/molecular layer deposition for energy storage and conversion, *Chem. Soc. Rev.* 50 (2021) 3889–3956, <https://doi.org/10.1039/D0CS00156B>.
- [4] Y. Huang, M. Zhu, Y. Huang, Z. Pei, H. Li, Z. Wang, Q. Xue, C. Zhi, Multifunctional energy storage and conversion devices, *Adv. Mater.* 28 (2016) 8344–8364, <https://doi.org/10.1002/adma.201601928>.
- [5] W. Li, J. Liu, D. Zhao, Mesoporous materials for energy conversion and storage devices, *Nat. Rev. Mater.* 1 (2016) 16023, <https://doi.org/10.1038/natrevmats.2016.23>.
- [6] X. Cao, C. Tan, M. Sindoro, H. Zhang, Hybrid micro-/nano-structures derived from metal-organic frameworks: preparation and applications in energy storage and conversion, *Chem. Soc. Rev.* 46 (2017) 2660–2677, <https://doi.org/10.1039/C6CS00426A>.
- [7] X. Li, S. Wang, L. Li, X. Zu, Y. Sun, Y. Xie, Opportunity of atomically thin two-dimensional catalysts for promoting CO_2 electroreduction, *Acc. Chem. Res.* 53 (2020) 2964–2974, <https://doi.org/10.1021/acs.accounts.0c00626>.
- [8] Z. Sun, T. Ma, H. Tao, Q. Fan, B. Han, Fundamentals and challenges of electrochemical CO_2 reduction using two-dimensional materials, *Chem* 3 (2017) 560–587, <https://doi.org/10.1016/j.chempr.2017.09.009>.
- [9] L. Cheng, Q. Xiang, Y. Liao, H. Zhang, CdS-Based photocatalysts, *Energy Environ. Sci.* 11 (2018) 1362–1391, <https://doi.org/10.1039/C7EE03640J>.
- [10] M. Han, S. Zhu, S. Lu, Y. Song, T. Feng, S. Tao, J. Liu, B. Yang, Recent progress on the photocatalysis of carbon dots: classification, mechanism and applications, *Nano Today* 19 (2018) 201–218, <https://doi.org/10.1016/j.nantod.2018.02.008>.
- [11] J. Zhang, X. Feng, Graphdiyne electrocatalyst, *Joule* 2 (2018) 1396–1398, <https://doi.org/10.1016/j.joule.2018.07.031>.
- [12] Y. Chen, H. Li, J. Wang, Y. Du, S. Xi, Y. Sun, M. Sherburne, J.W. Ager, A.C. Fisher, Z.J. Xu, Exceptionally active iridium evolved from a pseudo-cubic perovskite for oxygen evolution in acid, *Nat. Commun.* 10 (2019) 572, <https://doi.org/10.1038/s41467-019-08532-3>.
- [13] J. Wang, W. Liu, G. Luo, Z. Li, C. Zhao, H. Zhang, M. Zhu, Q. Xu, X. Wang, C. Zhao, Y. Qu, Z. Yang, T. Yao, Y. Li, Y. Lin, Y. Wu, Y. Li, Synergistic effect of well-defined dual site boosting oxygen reduction reaction, *Energy Environ. Sci.* 11 (2019) 3375–3379, <https://doi.org/10.1039/C8EE02656D>.
- [14] C.-T. Dinh, A. Jain, F.P.G. de Arquer, P. De Luna, J. Li, N. Wang, X. Zheng, J. Cai, B. Z. Gregory, O. Voznyy, B. Zhang, M. Liu, D. Sinton, E.J. Crumlin, E.H. Sargent, Multi-site electrocatalysts for hydrogen evolution in neutral media by destabilization of water molecules, *Nat. Energy* 4 (2018) 107–114, <https://doi.org/10.1038/s41560-018-0296-8>.
- [15] H. Chen, X. Liang, Y. Liu, X. Ai, T. Asefa, X. Zou, Active site engineering in porous electrocatalysts, *Adv. Mater.* 32 (2020) 2002435, <https://doi.org/10.1002/adma.202002435>.
- [16] J. Yin, J. Jin, H. Zhang, M. Lu, Y. Peng, B. Huang, P. Xi, C.-H. Yan, Atomic arrangement in metal doped NiS_2 boosts hydrogen evolution reaction in alkaline media, *Angew. Chem. Int. Ed.* 58 (2019) 18676–18682, <https://doi.org/10.1002/anie.201911470>.
- [17] J. Zhou, Y. Wang, X. Su, S. Gu, r Liu, Y. Huang, S. Yan, J. Li, s zhang, , Electrochemically accessing ultrathin Co (oxy)-hydroxide nanosheet and operando identifying its active phase for oxygen evolution reaction, *Energy Environ. Sci.* 12 (2019) 739–746, <https://doi.org/10.1039/C8EE03208D>.
- [18] L. Yu, L. Wu, B. McElhenny, S. Song, D. Luo, F. Zhang, Y. Yu, S. Chen, Z. Ren, Ultrafast room-temperature synthesis of porous S-doped Ni/Fe (oxy)hydroxide electrodes for oxygen evolution catalysis in seawater splitting, *Energy Environ. Sci.* 13 (2020) 3439–3446, <https://doi.org/10.1039/D0EE00921K>.
- [19] M. Ma, X. Han, H. Li, X. Zhang, Z. Zheng, L. Zhou, J. Zheng, Z. Xie, Q. Kuang, L. Zheng, Tuning electronic structure of PdZn nanocatalyst via acid-etching strategy for highly selective and stable electrolytic nitrogen fixation under ambient conditions, *Appl. Catal. B: Environ.* 265 (2019), 118568, <https://doi.org/10.1016/j.apcatb.2019.118568>.
- [20] J.S. Kanady, P. Leidinger, A. Haas, S. Titlbach, S. Schunk, K. Schierle-Armdt, E. J. Crumlin, C.H. Wu, A.P. Alivisatos, Synthesis of Pt_3Y and other early-late intermetallic nanoparticles by way of a molten reducing agent, *J. Am. Chem. Soc.* 139 (2017) 5672–5675, <https://doi.org/10.1021/jacs.7b01366>.
- [21] J. Cai, Y. Song, Y. Zang, S. Niu, Y. Wu, Y. Xie, X. Zheng, Y. Liu, Y. Lin, X. Liu, G. Wang, Y. Qian, N-induced lattice contraction generally boosts the hydrogen evolution catalysis of P-rich metal phosphides, *Sci. Adv.* 6 (2020) eaaw8113, <https://doi.org/10.1126/sciadv.aaw8113>.
- [22] M. Cong, D. Sun, L. Zhang, X. Ding, In situ assembly of metal-organic framework-derived N-doped carbon/Co/CoP catalysts on carbon paper for water splitting in alkaline electrolytes, *Chin. J. Catal.* 41 (2020) 242–248, [https://doi.org/10.1016/S1872-2067\(19\)63410-8](https://doi.org/10.1016/S1872-2067(19)63410-8).
- [23] X. Huang, Z. Zhao, L. Cao, Y. Chen, E. Zhu, Z. Lin, M. Li, A. Yan, A. Zettl, Y. M. Wang, X. Duan, T. Mueller, Y. Huang, High-performance transition

- metal-doped Pt₃Ni octahedra for oxygen reduction reaction, *Science* 348 (2015) 1230–1234, <https://doi.org/10.1126/science.aaa8765>.
- [24] H. Li, Y. Han, H. Zhao, W. Qi, D. Zhang, Y. Yu, W. Cai, S. Li, J. Lai, B. Huang, L. Wang, Fast site-to-site electron transfer of high-entropy alloy nanocatalyst driving redox electrocatalysis, *Nat. Commun.* 11 (2020) 5437, <https://doi.org/10.1038/s41467-020-19277-9>.
- [25] H. Zhao, D. Zhang, Z. Wang, Y. Han, X. Sun, H. Li, X. Wu, Y. Pan, Y. Qin, S. Lin, Z. Xu, J. Lai, L. Wang, High-performance nitrogen electroreduction at low overpotential by introducing Pb to Pd nanosponges, *Appl. Catal. B Environ.* 265 (2019), 118481, <https://doi.org/10.1016/j.apcatb.2019.118481>.
- [26] Y. Xie, J. Cai, Y. Wu, Y. Zang, X. Zheng, J. Ye, P. Cui, S. Niu, Y. Liu, J. Zhu, X. Liu, G. Wang, Y. Qian, Boosting water dissociation kinetics on Pt–Ni nanowires by N-induced orbital tuning, *Adv. Mater.* 31 (2019) 1807780, <https://doi.org/10.1002/adma.201807780>.
- [27] W. Cai, Y. Han, H. Li, W. Qi, J. Xu, X. Wu, H. Zhao, X. Zhang, J. Lai, L. Wang, Significantly enhanced electrocatalytic N₂ reduction to NH₃ by surface selenization with multiple functions, *J. Mater. Chem. A* 8 (2020) 20331–20336, <https://doi.org/10.1039/D0TA06991D>.
- [28] Y. Luo, L. Tang, U. Khan, Q. Yu, H.-M. Cheng, X. Zou, B. Liu, Morphology and surface chemistry engineering toward pH-universal catalysts for hydrogen evolution at high current density, *Nat. Commun.* 10 (2019) 269, <https://doi.org/10.1038/s41467-018-07792-9>.
- [29] Y. Yang, H. Yao, Z. Yu, S.M. Islam, H. He, M. Yuan, Y. Yue, K. Xu, W. Hao, G. Sun, H. Li, S. Ma, P. Zapol, M.G. Kanatzidis, Hierarchical nanoassembly of MoS₂/Co₉S₈/Ni₃S₂/Ni as a highly efficient electrocatalyst for overall water splitting in a wide pH range, *J. Am. Chem. Soc.* 141 (2019) 10417–10430, <https://doi.org/10.1021/jacs.9b04492>.
- [30] P.-C. Chen, M. Liu, J.S. Du, B. Meckes, S. Wang, H. Lin, V.P. Dravid, C. Wolverton, C.A. Mirkin, Interface and heterostructure design in polyelemental nanoparticles, *Science* 363 (2019) 959–964, <https://doi.org/10.1126/science.aav4302>.
- [31] X. Sun, N. Habibul, H. Du, Co_{0.85}Se magnetic nanoparticles supported on carbon nanotubes as catalyst for hydrogen evolution reaction, *Chin. J. Catal.* 42 (2021) 235–243, [https://doi.org/10.1016/S1872-2067\(20\)63632-4](https://doi.org/10.1016/S1872-2067(20)63632-4).
- [32] T. Li, D. Zhi, Y. Chen, B. Li, Z. Zhou, F. Meng, Multiaxial electrospun generation of hollow graphene aerogel spheres for broadband high-performance microwave absorption, *Nano Res.* 13 (2020) 477–484, <https://doi.org/10.1007/s12274-020-2632-0>.
- [33] W. Karim, C. Spreafico, A. Kleibert, J. Gobrecht, J. VandeVondele, Y. Ekinici, J. A. van Bokhoven, Catalyst support effects on hydrogen spillover, *Nature* 541 (2017) 68–71, <https://doi.org/10.1038/nature20782>.
- [34] Y. Yao, Z. Huang, P. Xie, S.D. Lacey, R.J. Jacob, H. Xie, F. Chen, A. Nie, T. Pu, M. Rehwoldt, D. Yu, M.R. Zachariah, C. Wang, R. Shahbazian-Yassar, J. Li, L. Hu, Carbothermal shock synthesis of high-entropy-alloy nanoparticles, *Science* 359 (2018) 1489–1494, <https://doi.org/10.1126/science.aan5412>.
- [35] W. Zhang, Y. Yang, B. Huang, F. Lv, K. Wang, N. Li, M. Luo, Y. Chao, Y. Li, Y. Sun, Z. Xu, Y. Qin, W. Yang, J. Zhou, Y. Du, D. Su, S. Guo, Ultrathin PtNiM (M = Rh, Os, and Ir) nanowires as efficient fuel oxidation electrocatalytic materials, *Adv. Mater.* 31 (2019) 1805833, <https://doi.org/10.1002/adma.201805833>.
- [36] D. Zhang, H. Zhao, B. Huang, B. Li, H. Li, Y. Han, Z. Wang, X. Wu, Y. Pan, Y. Sun, X. Sun, J. Lai, L. Wang, Advanced ultrathin RuPdM (M = Ni, Co, Fe) nanosheets electrocatalyst boosts hydrogen evolution, *ACS Cent. Sci.* 5 (2019) 1991–1997, <https://doi.org/10.1021/acscentsci.9b01110>.
- [37] X. Ai, X. Zou, H. Chen, Y. Su, X. Feng, Q. Li, Y. Liu, Y. Zhang, X. Zou, Transition-metal–boron intermetallics with strong interatomic d–sp orbital hybridization for high-performance electrocatalysis, *Angew. Chem. Int. Ed.* 59 (2020) 3961–3965, <https://doi.org/10.1002/anie.201915663>.
- [38] M. Sankar, N. Dimitratos, P.J. Miedziak, P.P. Wells, C.J. Kiely, G.J. Hutchings, Designing bimetallic catalysts for a green and sustainable future, *Chem. Soc. Rev.* 41 (2012) 8099–8139, <https://doi.org/10.1039/C2CS35296F>.
- [39] G. Zhang, B. Wang, J. Bi, D. Fang, S. Yang, Constructing ultrathin CoP nanomeses by Er-doping for highly efficient bifunctional electrocatalysts for overall water splitting, *J. Mater. Chem. A* 7 (2019) 5769–5778, <https://doi.org/10.1039/C9TA00530G>.
- [40] S.-H. Lee, V. Sridhar, J.-H. Jung, K. Karthikeyan, Y.-S. Lee, R. Mukherjee, N. Koratkar, I.-K. Oh, Graphene–nanotube–iron hierarchical nanostructure as lithiumion battery anode, *ACS Nano* 7 (2013) 4242–4251, <https://doi.org/10.1021/nn4007253>.
- [41] S. Xu, G. Zhong, C. Chen, M. Zhou, D.J. Kline, R.J. Jacob, H. Xie, S. He, Z. Huang, J. Dai, A.H. Brozena, R. Shahbazian-Yassar, M.R. Zachariah, S.M. Anlage, L. Hu, Uniform, scalable, high-temperature microwave shock for nanoparticle synthesis through defect engineering, *Matter* 1 (2019) 759–769, <https://doi.org/10.1016/j.matt.2019.05.022>.
- [42] H. Lu, W. Fan, Y. Huang, T. Liu, Lotus root-like porous carbon nanofiber anchored with CoP nanoparticles as all-pH hydrogen evolution electrocatalysts, *Nano Res.* 11 (2018) 1274–1284, <https://doi.org/10.1007/s12274-017-1741-x>.
- [43] Y. Wen, T. Yang, C. Cheng, X. Zhao, E. Liu, J. Yang, Engineering Ru(IV) charge density in Ru@RuO₂ core-shell electrocatalyst via tensile strain for efficient oxygen evolution in acidic media, *Chin. J. Catal.* 41 (2020) 1161–1167, [https://doi.org/10.1016/S1872-2067\(20\)63543-4](https://doi.org/10.1016/S1872-2067(20)63543-4).
- [44] D.H. Kweon, M.S. Okyay, S.-J. Kim, J.-P. Jeon, H.-J. Noh, N. Park, J. Mahmood, J.-B. Baek, Ruthenium anchored on carbon nanotube electrocatalyst for hydrogen production with enhanced Faradaic efficiency, *Nat. Commun.* 11 (2020) 1278, <https://doi.org/10.1038/s41467-020-15069-3>.
- [45] J. Mahmood, F. Li, S.-M. Jung, M.S. Okyay, I. Ahmad, S.-J. Kim, N. Park, H. Y. Jeong, J.-B. Baek, An efficient and pH-universal ruthenium-based catalyst for the hydrogen evolution reaction, *Nat. Nanotechnol.* 12 (2017) 441–446, <https://doi.org/10.1038/nnano.2016.304>.
- [46] T.W. van Deelen, C. Hernández Mejía, K.P. de Jong, Control of metal-support interactions in heterogeneous catalysts to enhance activity and selectivity, *Nat. Catal.* 2 (2019) 955–970, <https://doi.org/10.1038/s41929-019-0364-x>.
- [47] L. Zhang, Z.-L. Lang, Y.-H. Wang, H. Tan, H.-Y. Zang, Z. Kang, Y.-G. Li, Cable-like Ru/WNO@C nanowires for simultaneously high-efficient hydrogen evolution and low-energy consumption chlor-alkali electrolysis, *Energy Environ. Sci.* 12 (2019) 2569–2580, <https://doi.org/10.1039/C9EE01647C>.
- [48] N.C. Bigall, A.-K. Herrmann, M. Vogel, M. Rose, P. Simon, W. Carrillo-Cabrera, D. Dorfs, S. Kaskel, N. Gaponik, A. Eychmüller, Hydrogels and aerogels from noble metal nanoparticles, *Angew. Chem. Int. Ed.* 48 (2009) 9731–9734, <https://doi.org/10.1002/anie.200902543>.
- [49] Q. Wu, M. Luo, J. Han, W. Peng, Y. Zhao, D. Chen, M. Peng, J. Liu, F.M.F. de Groot, Y. Tan, Identifying electrocatalytic sites of nanoporous copper–ruthenium alloy for hydrogen evolution reaction in alkaline electrolyte, *ACS Energy Lett.* 5 (2020) 192–199, <https://doi.org/10.1021/acsenerylett.9b02374>.
- [50] J. Yu, Y. Guo, S. She, S. Miao, M. Ni, W. Zhou, M. Liu, Z. Shao, Bigger is surprisingly better: agglomerates of larger RuP nanoparticles outperform benchmark Ru nanocatalysts for the hydrogen evolution reaction, *Adv. Mater.* 30 (2018) 1800047, <https://doi.org/10.1002/adma.201800047>.
- [51] Z. Pu, I.S. Amiin, Z. Kou, W. Li, S. Mu, RuP₂-based catalysts with platinum-like activity and higher durability for the hydrogen evolution reaction at all pH values, *Angew. Chem. Int. Ed.* 56 (2017) 11559–11564, <https://doi.org/10.1002/anie.201704911>.
- [52] A. Velázquez-Palenzuela, F. Masini, A.F. Pedersen, M. Escudero-Escribano, D. Deiana, P. Malacrida, T.W. Hansen, D. Friebe, A. Nilsson, I.E.L. Stephens, I. Chorkendorff, The enhanced activity of mass-selected Pt_xGd nanoparticles for oxygen electroreduction, *J. Catal.* 328 (2015) 297–307, <https://doi.org/10.1016/j.jcat.2014.12.012>.
- [53] Y. Hu, J.O. Jensen, L.N. Cleemann, B.A. Brandes, Q. Li, Synthesis of Pt-rare earth metal nanoalloys, *J. Am. Chem. Soc.* 142 (2020) 953–961, <https://doi.org/10.1021/jacs.9b10813>.